

Statistics within UV–Visible Absorption Spectrum of Ethanolic Azobenzene

Eemeli A. Eronen* and Johannes Niskanen†

University of Turku, Department of Physics and Astronomy, FI-20014 Turun yliopisto, Finland

(Dated: February 6, 2026)

We report a statistical simulation of the UV–visible absorption spectrum of *trans*-azobenzene in ethanol solution. Due to intermolecular interactions, the used explicit solvent environment necessitates accounting for numerous transitions for a spectrum covering the two energetically lowest lines, S_1 and S_2 . Furthermore, the spectrum manifests vast variation as a function of the underlying local structure, in conjunction with previous observations for spectra of liquids in the X-ray regime. We disentangle the complex structure–spectrum relationship using a machine learning-based method known as the emulator-based component analysis. This structural decomposition outperforms commonly used principal component analysis in explained spectral variation and reveals a small subset of latent structural variables responsible for the total spectral variance. Among other structural characteristics, blueshifting of the S_2 peak occurs with fewer hydrogen bonds with the ethanol solvent, and a contracted N=N bond within the C–N=N–C bridge. The observed structural dependence of the absorption spectrum thus implies an overrepresentation of certain structural classes after a photoexcitation, potentially significant for the subsequent nuclear dynamics, photophysics, and photochemistry.

I. INTRODUCTION

A liquid system exhibits a wealth of local atomistic configurations, manifested as significant variation in *e.g.* its ensemble-averaged X-ray [1–5] and UV–visible [6–8] spectra. This underlying diversity is ignored when evaluating molecular properties for a single representative structure, and is probably impossible to capture by a few selected structures and their respective spectra [9]. Statistical variation of spectra implies pre-selection of structures for a spectral response, such as photon absorption at a given wavelength. At the same time, this structure-dependent response allows for structural characterization if the spectrally relevant structural degrees of freedom can be identified. In a liquid system, this is not trivial. To this end, extensive simulations allow an insight into the structure–spectrum relationship when combined with analysis techniques such as the recently introduced emulator-based component analysis (ECA) [10–13]. This method is used to identify the characteristics of the input \mathbf{x} , that are decisive for the response $\mathbf{y}(\mathbf{x})$, thus simplifying the inverse problem posed by structural (\mathbf{x}) interpretation of spectra (\mathbf{y}). Such target-variance-driven dimensionality reduction is also useful when the outcome \mathbf{y} depends predominantly on a small, unknown subset of features in a high-dimensional \mathbf{x} . The ECA method requires approximating $\mathbf{y}(\mathbf{x})$ by a reasonably accurate and computationally efficient emulator $\mathbf{y}_{\text{emu}}(\mathbf{x})$, for which a neural network is a contemporary choice. Potential applications of the protocol include, but are not limited to, statistical phenomena in molecular liquids and in their spectra, the topic of this work.

In this work, we study the UV–visible spectrum of *trans*-azobenzene in ethanol solution by combining

molecular dynamics (MD) simulations with subsequent spectral calculations and dimensionality reduction procedures. We find that the dominant structural variation in this complex system, derived by principal component analysis (PCA), does not explain the intensity behavior within key spectral regions. Instead, decomposition by ECA captures the spectral variance with just a few latent structural degrees of freedom, that cover a small fraction of the total structural spread. With this low-dimensional representation, we identify the most significant structural characteristics behind a shift in the S_2 peak. Finally, we discuss the implications of these findings for processes occurring after photoexcitation.

II. METHODS

We sampled 30 000 structures from extended tight binding MD (xTBMD) using the GFN1-xTB method [14, 15] implemented in the CP2K software [16] v. 2024.2. In the simulations, a *trans*-azobenzene molecule was dissolved in 159 ethanol molecules in a cubic box of $L = 25.04$ Å for the density 0.7840 g/cm³ interpolated for pure ethanol liquid at 300 K [17]. After equilibration of 20 ps, we sampled the canonical ensemble at 300 K with a 10 fs interval from a production run of 300 ps (for validation, see SI). We used a global Nosé–Hoover thermostat [18, 19] with chain length 3, a time constant τ of 1000 fs, and an MD timestep of 0.5 fs.

For evaluation of spectra consisting of 50 transitions on each of the 30 000 structures, we applied time-dependent density functional theory (TD-DFT) implemented in ORCA v.6.0.0 [20]. We explicitly included ethanol within the cutoff radius of 3.0 Å, and simulated this cluster in a conductor-like polarizable continuum model [21]. We used B3LYP exchange–correlation potential [22, 23], def2-SVP basis set [24] and def2/J auxiliary basis set [25] in the spectral simulations. We evaluated the cross section

* eemeli.a.eronen@utu.fi

† johannes.niskanen@utu.fi

σ_i of each transition i for a randomly oriented sample using the transition matrix element in the velocity form. We then convolved this stick spectrum to differential cross section $d\sigma/dE$ in terms of energy E by a Gaussian function (full-width at half maximum 0.414 eV), together with a constant shift of 0.300 eV in energy. We obtained these required parameters from a fit of the the computational ensemble-averaged spectrum to an experiment by Nägele and coworkers [26]. Finally, we transformed the differential cross section into wavelength λ scale for $d\sigma/d\lambda$. We use a constant convolution width in energy, because a constant width in wavelength makes the lines artificially broad for short wavelengths.

To capture the structure–spectrum relationship in these data, we train a neural network emulator and use it to iteratively find the ECA vectors for identifying spectrally decisive structural characteristics in the system. As the raw atomic coordinates from simulations are sub-optimal for machine learning, we preprocess the structural information using a local version of the many-body tensor representation (LMBTR) [27]. The LMBTR descriptor consists of Gaussian-smearred element-wise radial distance distributions for multiple centers in the system. As these centers, we use all the nitrogen and carbon sites in the azobenzene molecule, and eight additional virtual centers located perpendicular to a plane defined by nearby atoms in the azobenzene molecule. The first four virtual centers lie ± 2 Å from each nitrogen atom. The latter four centers lie ± 2 Å perpendicular from the arithmetic mean position of the *para* and *ortho* carbon atoms of each ring. For each structure, the encoding procedure resulted in a vector \mathbf{d} , which we z-score standardized to produce $\tilde{\mathbf{d}}$ used in machine learning and ECA. To establish a well-performing LMBTR–neural network combination, we ran a joint search [12] including both LMBTR and neural network hyperparameters, and chose the best-performing combination. The final model had an R^2 score (coefficient of determination) of 0.945 on a test set of 5 000 points, split from the data pool of 30 000 points prior to model selection, and thus previously unseen by the model. For more details, we refer to SI.

The ECA algorithm aims to identify a few spectrally most relevant structural degrees of freedom, ordered by their spectral significance. We project the z-score standardized structural feature vectors $\tilde{\mathbf{d}}$ of the test set onto the basis vectors \mathbf{v}_i . Thus, each basis vector results in a single latent coordinate t_i for a data point. Furthermore, an approximation

$$\tilde{\mathbf{d}}^{(k)} = \sum_{i=1}^k t_i \mathbf{v}_i \quad (1)$$

for each data point $\tilde{\mathbf{d}}$ is obtained in the given rank k . In the ECA procedure, vectors \mathbf{v}_i are tuned rank-by-rank to maximize the explained spectral variance for the neural network emulator prediction over all data $\tilde{\mathbf{d}}^{(k)}$. We first optimize the basis vectors for dimensionality reduction using the training set, and then apply this dimensionality

reduction in the analysis performed using the test set. The results of the analysis in the z-score standardized space can be converted to the original descriptor space by the corresponding inverse transform.

III. RESULTS

Figure 1a shows the simulated ensemble-averaged spectrum together with the experimental one by Nägele and coworkers [26]. We apply the molecular notation S_1 and S_2 for the characteristic features in this spectrum, but note that in our simulation for the gas phase in the optimized geometry, the S_2 line already has three underlying states. In liquid, we find the photoexcited states of *trans*-azobenzene to be mixed with states of the ethanol, which results in a wealth of possible final states to be excited – and to be simulated with explicit solvation. In our data, the average number of transitions within lines S_1 (390 nm–520 nm) and S_2 (270 nm–390 nm) were 0.9 and 14.1, respectively. The S_1 feature is almost unobservable, and we focus on the S_2 peak. We observe significant statistical variation between the spectra of individual local structures, as shown by the standard deviation σ in Figure 1a. For the following analysis, we define two regions of interest (ROI), split at the maximum of the S_2 peak. Then, we study the mean differential cross section within each ROI as a function of the structure. This practice makes the analysis focus on overall features of the contributing spectra within the peak, instead of their fine details, that are more prone to error due to the used approximations. We first train a neural network to predict the two z-score standardized ROI values for a structure, and then utilize this emulator in the ECA procedure for dimensionality reduction to identify the decisive structural characteristics behind the observed spectral variation.

The ECA method is analogous to PCA with the key difference being that the optimization target of the former is the explained ROI intensity variance. As seen in Figure 1b, rapid convergence towards the emulator performance limit is observed when emulation is carried out on data points projected onto the low-dimensional subspace. In contrast, applying PCA to the structural data points $\tilde{\mathbf{d}}$ aims at finding the decisive components of structural variance, not necessarily reflected by the spectral response as seen in Figure 1b. Vectors from structural PCA cover significantly less spectral variance after the corresponding evaluation. Perhaps even more notably, the dominant structural degree of freedom is spectrally irrelevant. The different optimization goal of the methods is also evident in the structural R^2 score as a function of the decomposition rank, presented in Figure 1c, which shows PCA to surpass the ECA decomposition. Thus, the majority of the spectral ROI intensity variance is explained by a minority of structural variance. We note that another method, partial least squares fitting, has previously been compared to ECA, with the latter excelling in this comparison [10].

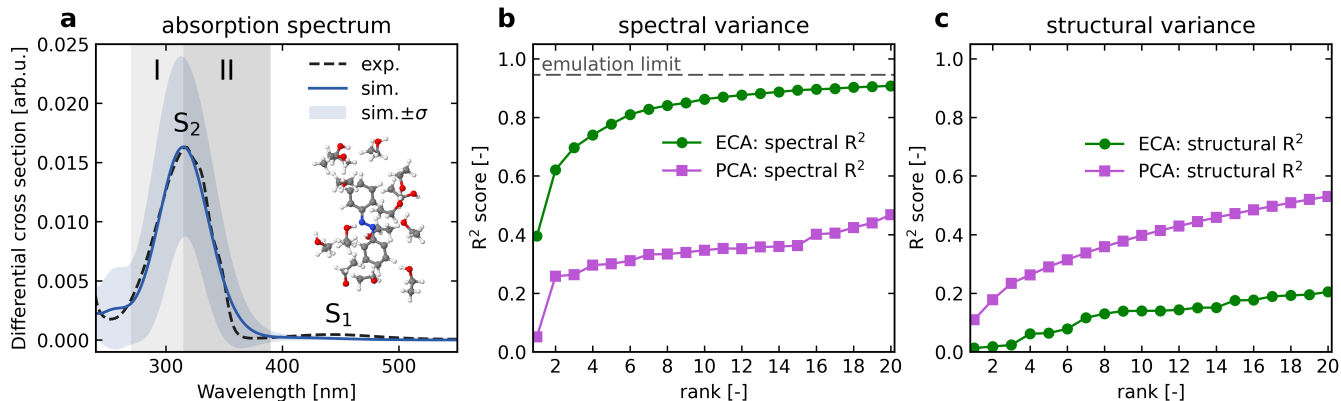


FIG. 1. Results of the spectrum calculations and variance captured by different dimensionality reduction techniques. **a**: Simulated ensemble average UV–visible absorption spectrum for *trans*-azobenzene in ethanol, together with an experiment reproduced from Ref. 26. The blue-shaded area depicts the standard deviation of the data set, indicating significant statistical variation. The gray-shaded areas depict the two regions of interest (ROIs I and II) defined for the subsequent analysis. Computational results have been shifted to match the experiment. Additionally, the figure presents an example local structure prepared with Jmol [28]. **b**: Spectral R^2 score as a function of the rank of emulator-based component analysis (ECA) and principal component analysis (PCA), evaluated using the neural network emulator after the respective dimensionality reduction. The first two ECA components explain a large portion of the spectral ROI variance, while the higher components show rapidly diminishing R^2 score gains. Structural decomposition by PCA covers significantly less spectral variance for the same rank. **c**: Structural R^2 score as a function of decomposition rank. The ECA vectors cover a small fraction of the structural variance compared to structural PCA. The result indicates that explaining structural variation alone does not explain the spectral variation.

Next, we turn to the analysis of the first two ECA component vectors, that indicate the structural changes responsible for most spectral ROI intensity variation. We first analyze the spectral effect, and then the associated structural changes. We define two spectral properties: (i) ROI value difference (ROI I – ROI II), and (ii) total ROI value sum. These properties can be directly linked in the two latent coordinates t_1 and t_2 , as indicated in Figure 2. The spectrally most significant structural degree of freedom t_1 corresponds to the ROI value difference (Figure 2a), whereas the second most significant degree of freedom t_2 captures the ROI value sum (Figure 2d). The two properties are mostly independent of each other, illustrated by the low cross-correlation in Figures 2b and 2c. From Figures 2a and 2d we conclude that ROI I intensity is high when t_1 and t_2 values are high. Similarly, ROI II intensity is high when t_1 value is low and t_2 high. Thus, the structural changes causing a blueshift of the S_2 line are indicated by the latent coordinate t_1 , as the effects from the second ECA component cancel out. For a structural interpretation of such effect, we calculate the difference $10 \mathbf{v}_1$ for a well-expected change in this coordinate, and then transform the respective ECA component vector to the original descriptor space. A further division by the squared distance to a corresponding center yields site-wise and element-wise curves with radial behavior proportional to that of the radial distribution function.

Figure 3 shows a selection of curves from the aforementioned comparison. The shorter-wavelength ROI I favors structures with less hydrogen bonding between the nitrogen atoms of *trans*-azobenzene and the OH group of

the ethanol solvent. This is evident from the reduction of hydrogen and oxygen in the curves with an azobenzene N at the origin. This is accompanied by an increase of carbon near the nitrogen center, which we interpret as rotation of the ethanol molecule. Moreover, a blueshift is indicative of shorter N=N and C_{N=N}-*ortho*-carbon bond lengths. The simultaneous reduction of N–C curves in short ranges indicates a shift towards longer N–C_{N=N} bond lengths at the azobenzene C–N=N–C bridge. The results were consistent across ten of the best-performing descriptor–neural network architecture combinations.

While the ECA procedure is carried out without *a priori* assumptions, the sanity of the obtained results can be confirmed *a posteriori* by evaluating the mean spectra for structures differing in the according characteristics. Using the whole data set, Figure 4 shows a blueshift of the S_2 peak for structures with shorter N=N bond lengths and for structures with less hydrogen bonds for N atoms, evaluated using geometric criteria [4]. We note that other notable structural changes are implied as well, and refer to the SI for the complete list.

Additionally, we performed a corresponding analysis for the total ROI value sum, the results of which are presented in the SI. This spectral property appears to be affected, for example, increase in the amount of the ethanol solvent near the very tips of the carbon rings. The result can be affected by a molecule being excluded from the explicitly treated cluster due to the necessitated cutoff distance, but is still indicative of a closer ethanol molecule. The analysis also suggests that numerous other less interpretable structural features affect the ROI value

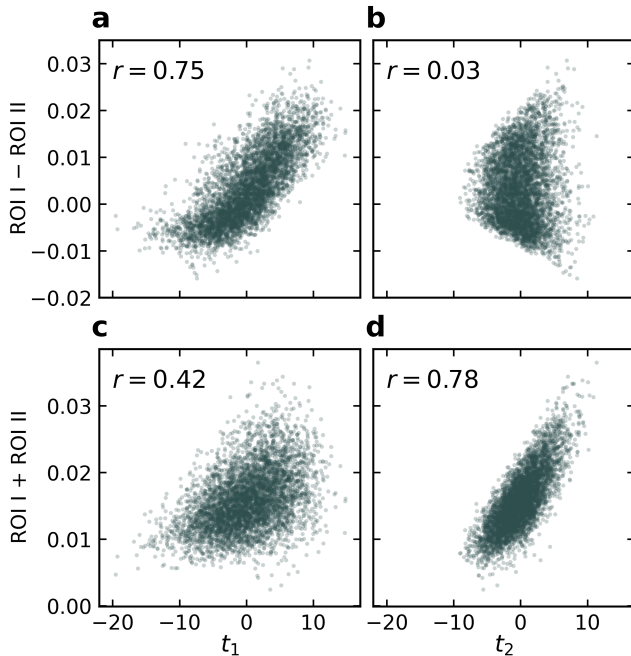


FIG. 2. The relationship between spectral properties and the latent coordinates from ECA using the test set with the corresponding Pearson’s correlation coefficients r . **a**: The difference between the two ROI values is highly correlated with the spectrally most significant structural variable t_1 . **b**: The correlation between ROI value difference and the second most significant structural variable t_2 is negligible. **c**: The total ROI value sum is weakly correlated with t_1 , but **d**: highly correlated with t_2 . For details, see text.

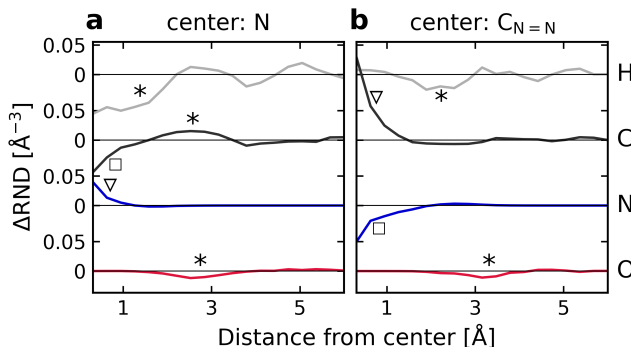


FIG. 3. Element-wise change in radial number density (ΔRND) implied by a ten-unit rise of latent coordinate t_1 associated with ROI value difference from **a**: the nitrogen atoms, and from **b**: carbon atoms of the $\text{C}_N=\text{N}-\text{C}$ bridge. We denote regions corresponding to the weakening of the hydrogen bonding and possible rotation of the ethanol molecules with an asterisk (*). Additionally, the triangles (∇) denote regions indicating shortening of $\text{N}=\text{N}$ or $\text{C}_N=\text{N}-\text{C}$ bonds, and the square (\square) denotes a region indicating an increase in the length of the $\text{N}-\text{C}$ bond. The curves shown are an average for the two N atoms or the two $\text{C}_N=\text{N}$ atoms.

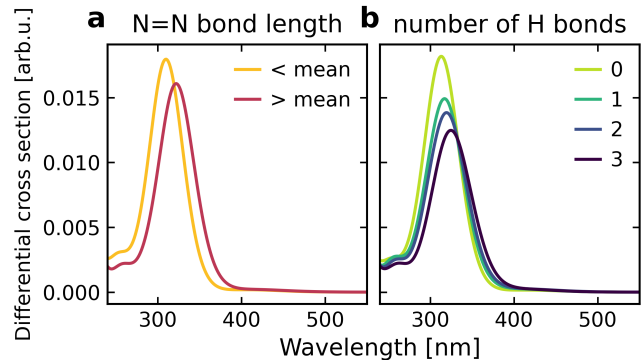


FIG. 4. Validation of the ECA results evaluated over the whole data set. **a**: The mean spectra of structures with $\text{N}=\text{N}$ bond length above and below the average value. **b**: The mean spectra for structures with a given number of hydrogen bonds accepted by the azo group, calculated with criteria described in Ref. [4]. The inspection is motivated by ECA first finding these characteristics.

sum.

We repeated the calculations using the PBE exchange–correlation potential [29], which in this case required evaluating 100 transitions. The aforementioned structural conclusions remain unaffected in the subsequent analysis, performed in a manner analogous to the presented one and reported in SI.

IV. DISCUSSION

The observed strong statistical variation of the UV–visible spectrum highlights the importance of proper ensemble sampling for the analysis of spectra of liquid systems. In this case, the variation is similar, if not greater, to what has been reported for X-ray spectra of liquids [2, 4, 12, 13, 30]. Furthermore, our analysis shows that the spectrum is affected by a wide range of structural properties, as a multitude of features in the ECA curves were non-zero (see Figure 3 and Supplementary Information). In spite of the large number of involved features, we emphasize that this subspace still covers a relatively small fraction of the total structural variance, as indicated in Figures 1b and 1c. Last, the fact that the ECA curves show a contribution from oxygen atoms is a direct indication that the ethanol solvent has a significant effect on the spectrum.

During preliminary studies, we found that relatively large neural networks without regularization outperformed smaller or regularized ones. Interestingly, funnel-shaped neural networks with a linearly decreasing number of neurons at each layer seemed to allow for sufficient complexity while using less resources than their rectangle-shaped counterparts of uniform width. These large networks had a tendency to heavily overfit to the training data while still generalizing well to the vali-

dation data and, eventually, the test data. This phenomenon is likely an example of a machine learning model reaching the interpolating regime with emergent self-regularization capability [31]. In contrast, the model selection in our previous works with X-ray spectra favored simpler architectures [5, 12, 13]. Furthermore, compared to the X-ray regime, a larger number of LMBTR centers with some virtual sites are necessary for sufficient machine learning performance for the UV–visible spectrum of ethanolic *trans*-azobenzene. While the structure–spectrum relation in the X-ray regime is not necessarily straightforward, these results are a strong indication of an even greater complexity of UV–visible spectra. The conclusion is reasonable in the sense that both orbitals involved in the transition matrix element extend over a large volume, whereas the core-orbital participating in an X-ray process is quite localized.

The presented simulations necessitated numerous approximations. For example, the cutoff value for the explicit solvent is an obvious one. We chose the cutoff to be as large as possible while still enabling the simulation of $\sim 10^4$ structure–spectrum pairs. Applying different methods for structural simulation and for property evaluation causes a bias in the results, but the practice is common in spectroscopy and quantum chemistry. In the case of this work, the MD run for the whole simulation cell would not be viable using the electronic structure method of the spectrum calculations. Additionally, we ignore the possible spectral effects arising from vibrational states. Despite this, the reasonability of our data is supported by the fact that the general shape of the spectrum agrees with the experiment. We also note that while switching from the B3LYP to the PBE exchange–correlation potential introduces more transitions (including possible ghost states) and slight changes in the spectra, the discussed structural dependencies of the ROI intensities are consistent across both models.

The challenges and limitations of the ECA method have been discussed in detail in Ref. 13. Most notably, the interpretation of the ECA results is dependent on the properties of the descriptor, intended to encode all information required to predict a spectrum for a structure. While numerous alternatives exist, the LMBTR descriptor excelled in a comparison of six structural descriptor families for X-ray spectra [12], and the performance obtained in the current work for UV–visible aligns well with these earlier results [5, 12, 13]. Further discussion on the required criteria for spectral interpretation by the protocol is available in Ref. 5. In a nutshell, the descriptor must allow good machine learning and ECA performance, and also be interpretable by a human. Development of a new, highly interpretable, atomistic descriptor for machine learning can have a significant positive impact on the method in the future.

Instead of representing two specific atomistic structures, the curves in Figure 3 reflect shifts in the structural distributions between the two selected points in the latent coordinate space. While not necessarily always

the case, for the UV–visible spectrum of ethanolic *trans*-azobenzene, the two latent coordinates link the respective structural classes to a shift of the S_2 peak, and reveal potentially important implications for photoprocesses in liquids. Namely, as a consequence of the observed spectral behaviour, the used excitation wavelength introduces a preference for certain initial structures for the following photodynamics, potentially observable by, *e.g.*, pump–probe experiments. Solvent properties have also been found to have an effect on the photochemistry of azobenzene [32], which could partially be a manifestation of this pre-selection.

V. CONCLUSIONS

The UV–visible absorption spectrum of ethanolic *trans*-azobenzene shows a broad statistical variation analogous to that found in X-ray spectra. Our subsequent analysis condensed the spectral variance to a few structural degrees of freedom, enabling a partial interpretation of the complex structure–spectrum relationship. We found that photon excitation on the short-wavelength side of the S_2 peak favors structures with, among other characteristics, weaker hydrogen bonding with the ethanol solvent, and a contraction of the N=N bond. Thus, the chosen incident photon energy may favor certain structures for the following photodynamics.

DATA AVAILABILITY

The data and relevant scripts are available in Zenodo: [10.5281/zenodo.15349624](https://zenodo.org/record/15349624).

CONFLICTS OF INTEREST

There are no conflicts to declare.

ACKNOWLEDGEMENTS

We acknowledge CSC – IT Center for Science, Finland, for providing computing resources. We thank Dr. N. Runeberg at CSC for support with the Puhti supercomputer, and Prof. J. Wachtveitl for providing the experimental UV–visible absorption spectrum of *trans*-azobenzene in ethanol solution. J.N. acknowledges funding by Research council of Finland via the academy project grant 367978.

- [1] P. Wernet, D. Nordlund, U. Bergmann, M. Cavalleri, M. Odellius, H. Ogasawara, L. Å. Näslund, T. K. Hirsch, L. Ojamäe, P. Glatzel, L. G. M. Pettersson, and A. Nilsson, The Structure of the First Coordination Shell in Liquid Water, *Science* **304**, 995 (2004).
- [2] N. Ottosson, K. J. Børve, D. Spångberg, H. Bergersen, L. J. Sæthre, M. Faubel, W. Pokapanich, G. Öhrwall, O. Björneholm, and B. Winter, On the Origins of Core-Electron Chemical Shifts of Small Biomolecules in Aqueous Solution: Insights from Photoemission and *ab Initio* Calculations of Glycineaq, *Journal of the American Chemical Society* **133**, 3120 (2011).
- [3] J. Niskanen, C. J. Sahle, K. O. Ruotsalainen, H. Müller, M. Kavčič, M. Žitnik, K. Bučar, M. Petric, M. Hakala, and S. Huotari, Sulphur $K\beta$ emission spectra reveal protonation states of aqueous sulfuric acid, *Scientific Reports* **6**, 21012 (2016).
- [4] J. Niskanen, C. J. Sahle, K. Gilmore, F. Uhlig, J. Smitatek, and A. Föhlisch, Disentangling Structural Information From Core-level Excitation Spectra, *Physical Review E* **96**, 013319 (2017).
- [5] E. A. Eronen, A. Vladyka, F. Gerbon, C. J. Sahle, and J. Niskanen, Information bottleneck in peptide conformation determination by x-ray absorption spectroscopy, *Journal of Physics Communications* **8**, 025001 (2024).
- [6] I. Timrov, M. Micciarelli, M. Rosa, A. Calzolari, and S. Baroni, Multimodel Approach to the Optical Properties of Molecular Dyes in Solution, *Journal of Chemical Theory and Computation* **12**, 4423 (2016).
- [7] F. C. Bononi, Z. Chen, D. Rocca, O. Andreussi, T. Hullar, C. Anastasio, and D. Donadio, Bathochromic Shift in the UV–Visible Absorption Spectra of Phenols at Ice Surfaces: Insights from First-Principles Calculations, *The Journal of Physical Chemistry A* **124**, 9288 (2020).
- [8] Z. Chen, F. C. Bononi, C. A. Sievers, W.-Y. Kong, and D. Donadio, UV–Visible Absorption Spectra of Solvated Molecules by Quantum Chemical Machine Learning, *Journal of Chemical Theory and Computation* **18**, 4891 (2022).
- [9] S. Gómez, P. Lafiosca, and T. Giovannini, Modeling UV/Vis Absorption Spectra of Food Colorants in Solution: Anthocyanins and Curcumin as Case Studies, *Molecules* **29**, 4378 (2024).
- [10] J. Niskanen, A. Vladyka, J. Niemi, and C. J. Sahle, Emulator-based decomposition for structural sensitivity of core-level spectra, *Royal Society Open Science* **9**, 220093 (2022).
- [11] A. Vladyka, C. J. Sahle, and J. Niskanen, Towards structural reconstruction from X-ray spectra, *Physical Chemistry Chemical Physics* **25**, 6707 (2023).
- [12] E. A. Eronen, A. Vladyka, C. J. Sahle, and J. Niskanen, Structural descriptors and information extraction from X-ray emission spectra: aqueous sulfuric acid, *Physical Chemistry Chemical Physics* **26**, 22752 (2024).
- [13] E. A. Eronen, A. Vladyka, C. J. Sahle, and J. Niskanen, Structural Sensitivity of N 1s Excitations in N-Methylacetamide Solutions, *The Journal of Physical Chemistry Letters* **16**, 1666 (2025).
- [14] S. Grimme, C. Bannwarth, and P. Shushkov, A Robust and Accurate Tight-Binding Quantum Chemical Method for Structures, Vibrational Frequencies, and Noncovalent Interactions of Large Molecular Systems Parametrized for All spd-Block Elements ($Z = 1-86$), *Journal of Chemical Theory and Computation* **13**, 1989 (2017).
- [15] C. Bannwarth, E. Caldeweyher, S. Ehlert, A. Hansen, P. Pracht, J. Seibert, S. Spicher, and S. Grimme, Extended tight-binding quantum chemistry methods, *WIREs Computational Molecular Science* **11**, e1493 (2021).
- [16] T. D. Kühne, M. Iannuzzi, M. Del Ben, V. V. Rybkin, P. Seewald, F. Stein, T. Laino, R. Z. Khatullin, O. Schütt, F. Schiffmann, D. Golze, J. Wilhelm, S. Chulkov, M. H. Bani-Hashemian, V. Weber, U. Borštnik, M. TAILLEFUMIER, A. S. Jakobovits, A. Lazaro, H. Pabst, T. Müller, R. Schade, M. Guidon, S. Andermatt, N. Holmberg, G. K. Schenter, A. Hehn, A. Bussy, F. Belleflamme, G. Tabacchi, A. Glöß, M. Lass, I. Bethune, C. J. Mundy, C. Plessl, M. Watkins, J. Vandevondele, M. Krack, and J. Hutter, CP2K: An electronic structure and molecular dynamics software package - Quickstep: Efficient and accurate electronic structure calculations, *The Journal of Chemical Physics* **152**, 194103 (2020).
- [17] I. S. Khattab, F. Bandarkar, M. A. A. Fakhree, and A. Jouyban, Density, viscosity, and surface tension of water+ethanol mixtures from 293 to 323K, *Korean Journal of Chemical Engineering* **29**, 812 (2012).
- [18] S. Nose, A unified formulation of the constant temperature molecular dynamics methods, *The Journal of Chemical Physics* **81**, 511 (1984).
- [19] S. Nose, A molecular dynamics method for simulations in the canonical ensemble, *Molecular Physics* **52**, 255 (1984).
- [20] F. Neese, Software update: The ORCA program system—Version 5.0, *WIREs Computational Molecular Science* **12**, e1606 (2022).
- [21] M. Garcia-Ratés and F. Neese, Effect of the Solute Cavity on the Solvation Energy and its Derivatives within the Framework of the Gaussian Charge Scheme, *Journal of Computational Chemistry* **41**, 922 (2020).
- [22] C. Lee, W. Yang, and R. G. Parr, Development of the Colle-Salvetti correlation-energy formula into a functional of the electron density, *Phys. Rev. B* **37**, 785 (1988).
- [23] A. D. Becke, Density-functional thermochemistry. III. The role of exact exchange, *The Journal of Chemical Physics* **98**, 5648 (1993).
- [24] F. Weigend and R. Ahlrichs, Balanced basis sets of split valence, triple zeta valence and quadruple zeta valence quality for H to Rn: Design and assessment of accuracy, *Physical Chemistry Chemical Physics* **7**, 3297 (2005).
- [25] F. Weigend, Accurate Coulomb-fitting basis sets for H to Rn, *Physical Chemistry Chemical Physics* **8**, 1057 (2006).
- [26] T. Nägele, R. Hoche, W. Zinth, and J. Wachtveitl, Femtosecond photoisomerization of cis-azobenzene, *Chemical Physics Letters* **272**, 489 (1997).
- [27] H. Huo and M. Rupp, Unified representation of molecules and crystals for machine learning, *Machine Learning: Science and Technology* **3**, 045017 (2022).
- [28] Jmol development team, Jmol: an open-source Java viewer for chemical structures in 3D, accessed: January 21, 2025.

- [29] J. P. Perdew, K. Burke, and M. Ernzerhof, Generalized gradient approximation made simple, *Physical Review Letters* **77**, 3865 (1996).
- [30] V. Vaz da Cruz, F. Gel'mukhanov, S. Eckert, M. Iannuzzi, E. Ertan, A. Pietzsch, R. C. Couto, J. Niskanen, M. Fondell, M. Dantz, T. Schmitt, X. Lu, D. McNally, R. M. Jay, V. Kimberg, A. Föhlisch, and M. Odelius, Probing Hydrogen Bond Strength in Liquid Water by Resonant inelastic X-ray scattering, *Nature Communications* **10**, 1013 (2019).
- [31] M. Belkin, D. Hsu, S. Ma, and S. Mandal, Reconciling modern machine-learning practice and the classical bias–variance trade-off, *Proceedings of the National Academy of Sciences* **116**, 15849 (2019).
- [32] H. M. D. Bandara and S. C. Burdette, Photoisomerization in different classes of azobenzene, *Chemical Society Reviews* **41**, 1809 (2012).

SUPPLEMENTARY INFORMATION

A. Validation of the molecular dynamics calculations

To validate the sampling of the molecular dynamics simulations, we evaluated autocorrelation functions of the production run sampled at 10 fs intervals. Figure 5 shows the autocorrelation for ROI intensities, LMBTR vectors, and full spectra. The curves for the ROI values and the full spectra show a rapid initial drop, indicating low correlation even for two temporally subsequent sampled data points. Therefore, the structure–spectrum data set used in this work consists of mostly uncorrelated data points even if the structural autocorrelation decays slower than its spectral counterpart.

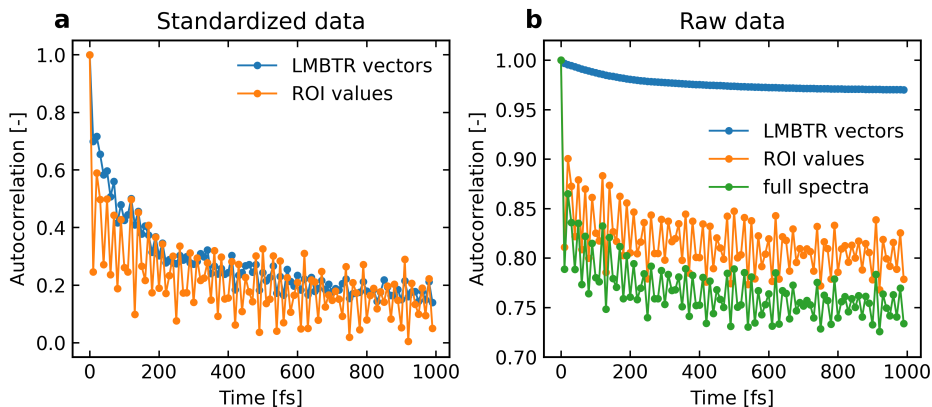


FIG. 5. Autocorrelation functions of the production run at intervals of 10 fs. **a**: The curves for z-score standardized data which was used in the analysis. Spectral data is represented by the two regions of interest values (ROIs) and the structural data is represented by the local many-body tensor representation (LMBTR) vectors derived from the xyz-coordinates and atomic number of each nucleus. **b** Corresponding curves for data that has not been z-score standardized. Additionally, we show the autocorrelation of the full spectra.

B. Machine learning details

We split the data set of 30 000 structure–spectrum pairs into three parts: (i) a training set of 24 000 points for training the neural network and fitting the ECA vectors, (ii) a validation set of 1 000 points for early stopping of neural network training and (iii) a test set of 5 000 points for testing the model and ECA. For the performance metric we chose the coefficient of determination or R^2 score which represents the spectral variance covered by the model. An R^2 score of 1 refers to perfect prediction performance whereas a value of 0 refers to performance where the model always predicts the mean of the data set. We z-score standardized the LMBTR vectors and the ROI values before any machine learning tasks. This means that we subtracted the according training data mean from each of the vector components, after which we divided the values by their standard deviations in the training set.

As the machine learning model we chose a fully connected feed-forward neural network emulator implemented using PyTorch¹. As illustrated in Figure 6, we used funnel-shaped neural networks with linearly decreasing number of neurons at each layer (excluding the input layer). Both the descriptor and the neural network have a wide range of tunable hyperparameters. Therefore, we ran a joint hyperparameter search² including both the descriptor and neural network hyperparameters as presented in Table I. We trained the models to predict the z-score standardized ROI intensities in mini-batches of 512 points each. The training was stopped if the performance on the separate early stopping data set of 1 000 points did not improve in 10 consecutive epochs. We used the rectified linear unit activation function and the Adam optimizer with an initial learning rate of 10^{-3} to minimize the R^2 loss (equals $1 - R^2$ score).

¹ A. Paszke *et al.* PyTorch: An Imperative Style, High-Performance Deep Learning Library. *Advances in Neural Information Processing Systems* 32, 8024–8035, 2019. url:<https://dl.acm.org/doi/10.5555/3454287.3455008>.

² E. A. Eronen, A. Vladyka, Ch. J. Sahle, and J. Niskanen. Structural descriptors and information extraction from X-ray emission spectra: aqueous sulfuric acid. *Physical Chemistry Chemical Physics*, 26:22752–22761, 2024. doi:10.1039/D4CP02454K.

For selection of the best combination of hyperparameters, we used five-fold cross-validation using the aforementioned training method to evaluate the performance of each trial model. In the end, we chose the model with the best mean cross-validation R^2 score and trained the final model using the full training data of 24000 data points.

For ECA we used the implementation by Vladyka *et al.*³. To ensure that a proper minimum is found, we fitted the each ECA vector 25 times with different initial guesses and chose the one with best performance before proceeding with the optimization of the next vector.

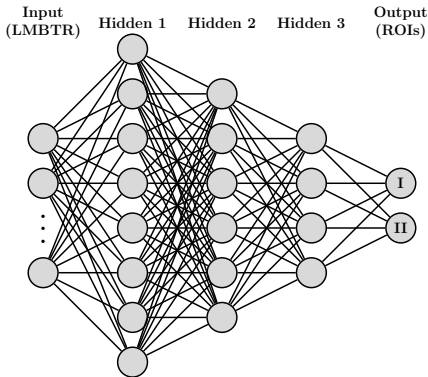


FIG. 6. A schematic of a funnel-shaped neural network used in this work.

TABLE I. The grid for the joint search of the LMBTR and neural network (NN) hyperparameters. The best performing combination is indicated in bold face.

	Hyperparameter	Grid points
LMBTR	grid min, \AA	{ 0 }
	grid max, \AA	{4, 5, 6 , 7}
	number of grid points	{ 20 , 40}
NN	Gaussian width, \AA	{0.4, 0.6 , 0.8, 1.0}
	weight decay	{ 0 }
	number of hidden layers	{2, 3 , 4, 5, 6}
	width of the first hidden layer	{1024, 2048 , 4096, 8192, 16384}

³ A. Vladyka, E. A. Eronen, and J. Niskanen, Implementation of the emulator-based component analysis, *Journal of Computa-*

C. A schematic of all LMBTR centers

Figure 7 shows a schematic of all the centers that we included in the LMBTR descriptor. The notation is used throughout the analysis of the structure–spectrum relationship. In the main text, we show the average of element-wise curves centered at N0 and N1, and the average of element-wise curves centered at C5 and C8.

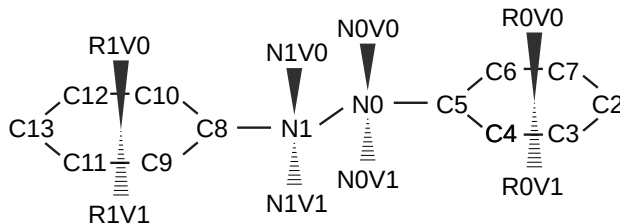


FIG. 7. A schematic of the centers for the LMBTR descriptor of the azobenzene molecule. We chose all the nitrogen and carbon atoms of the molecule and a set of eight virtual points (V) as centers. The first four are located $\pm 2 \text{ \AA}$ off-plane from the nitrogen atoms, with the plane defined by three nearby atoms (N1, N0 and C5, or N0, N1 and C8). The latter four are located $\pm 2 \text{ \AA}$ off-plane from the carbon rings (R), with the plane defined by the two *ortho*-carbon atoms (C4 and C6, or C9 and C10) and a *para*-carbon atom (C2 or C13).

D. ROI value difference with large overall intensity: full list of structural changes

Figure 8 shows the complete list of structural changes implied by a blueshift in the S_2 peak, according to the applied analysis procedure. The vector, originally in the z-score-standardized descriptor space, has been inverse transformed to the original descriptor space after which each feature has been divided by the squared distance to the corresponding center. In addition to the results discussed in the main text, the curves at centers C2 and C13 indicate shortening of the *para*-carbon–*meta*-carbon bonds. Other less interpretable effects are also implied by the curves; for example, the hydrogen and carbon curves of the virtual centers. We note that the large absolute values near zero exhibited by some of the curves of the virtual centers are an artifact originating from the division by the squared distance to the center.

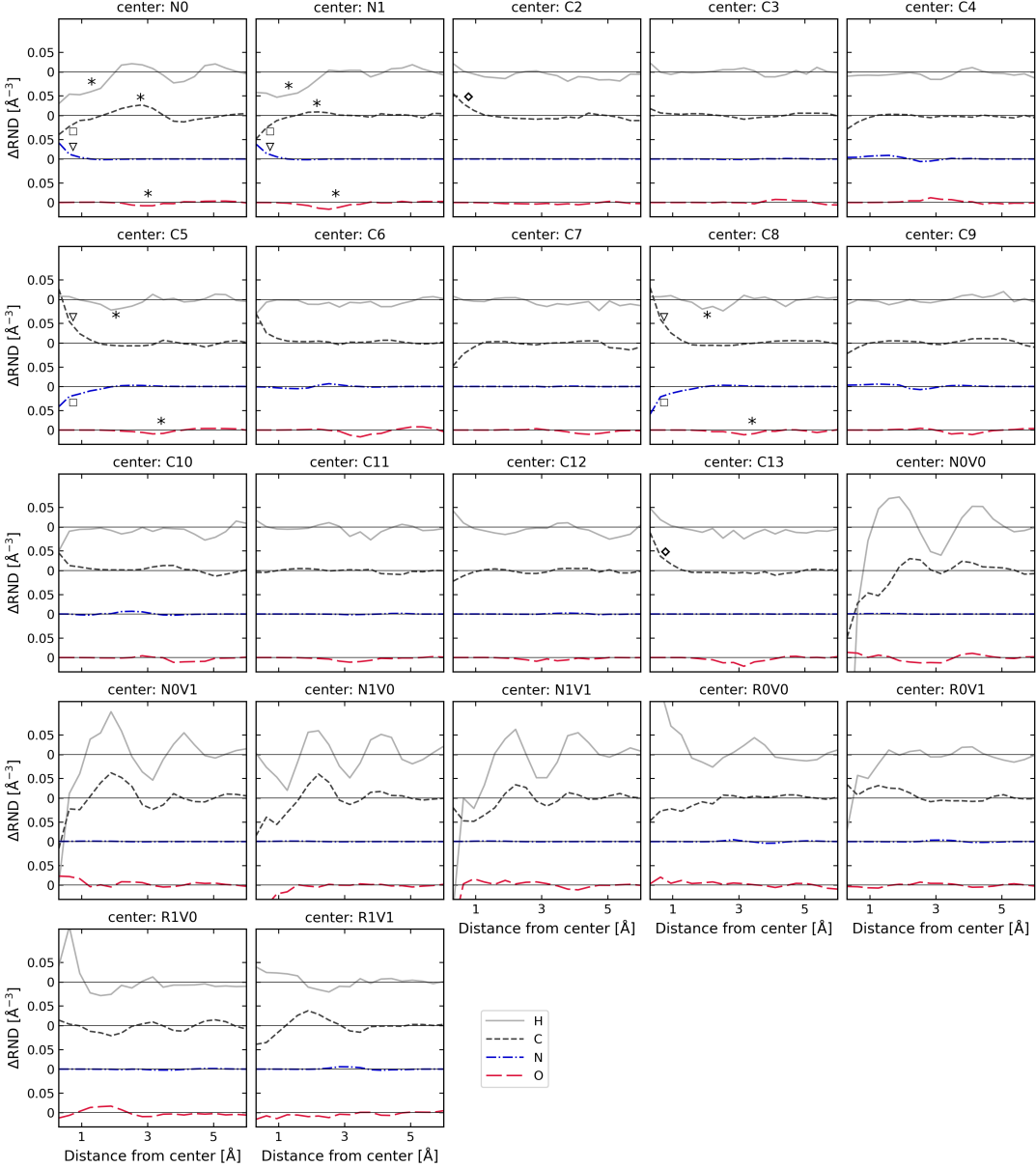


FIG. 8. The full LMBTR vector corresponding to the structural shift behind the increase of the ROI value difference. We denote regions corresponding to weakening of hydrogen bonds with an asterisk (*), shortening of N=N bond with triangles (∇), shortening of C-C bonds with diamonds (◇), and increase in the N-C bond lengths with squares (□). Numerous other less interpretable factors also play a role in the structure–spectrum relationship.

E. Structural changes implied by the increase of total ROI value

Similarly to the analysis of the ROI value difference, Figure 9 shows the complete list of structural changes implied by an increase in the total ROI value, *i.e.* the sum of the average differential cross section within each ROI. Again, several structural factors affect the spectrum, some being more interpretable than others. The ROI sum is affected by, for example, an increase in the amount of the ethanol solvent near the very tips of the carbon rings. The result can be affected by a molecule being excluded from the explicitly treated cluster due to the necessitated cutoff distance, but is still indicative of a closer ethanol molecule.

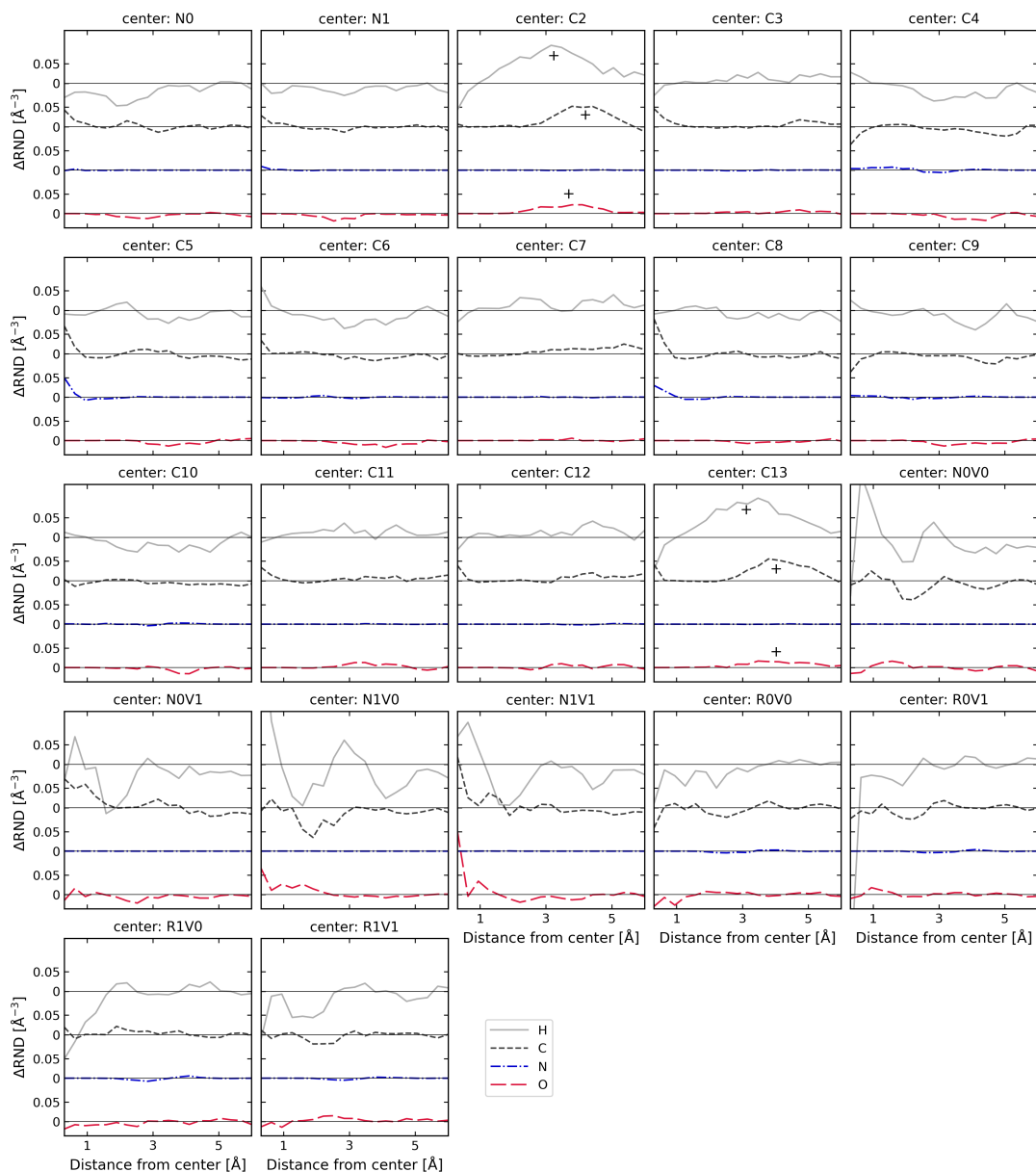


FIG. 9. The full LMBTR vector corresponding to the structural shift behind the increase in total ROI value. We denote regions corresponding to the increase in the amount of ethanol solvent near the tips of the azobenzene rings with plus signs (+). Many other less interpretable factors also play a role in the structure–spectrum relationship.

F. Results using spectra calculated with the PBE exchange-correlation potential

In the main text we studied regions of interest derived from spectra calculated using the B3LYP functional. Here we present the corresponding results using spectra calculated with the PBE exchange-correlation potential. Figure 10 shows the ensemble averaged spectrum, where each line of the individual spectra is convolved with a Gaussian of full-width at half maximum of 0.370 eV and shifted by 0.527 eV. Analogous to the case of B3LYP in the main text, we obtained these values by a fitting the ensemble-averaged spectrum on the experiment by Nägele and coworkers⁴. Especially at the low-wavelength tail of the S_2 peak, the simulated spectrum approximates the experiment less well than the corresponding spectrum calculated with B3LYP. The R^2 score behavior of the ECA decomposition is similar between the two cases, with the spectral R^2 score rising slightly faster with PBE. Figure 11 shows that the first two ECA components show the similar behavior with either of the functionals, except the order of the vectors one and two are flipped. Figure 12 shows that curves denoting structural changes behind a blueshift in the spectrum show highly similar behavior to that found in the main text. Therefore, the qualitative conclusions of the main text are the same for PBE and B3LYP. The different behavior at short distances is likely due to the different LMBTR Gaussian widths originating from the independent model selections performed for B3LYP and PBE data. Figure 13 confirms the consistency in terms of N=N bond lengths and the number of hydrogen bonds.

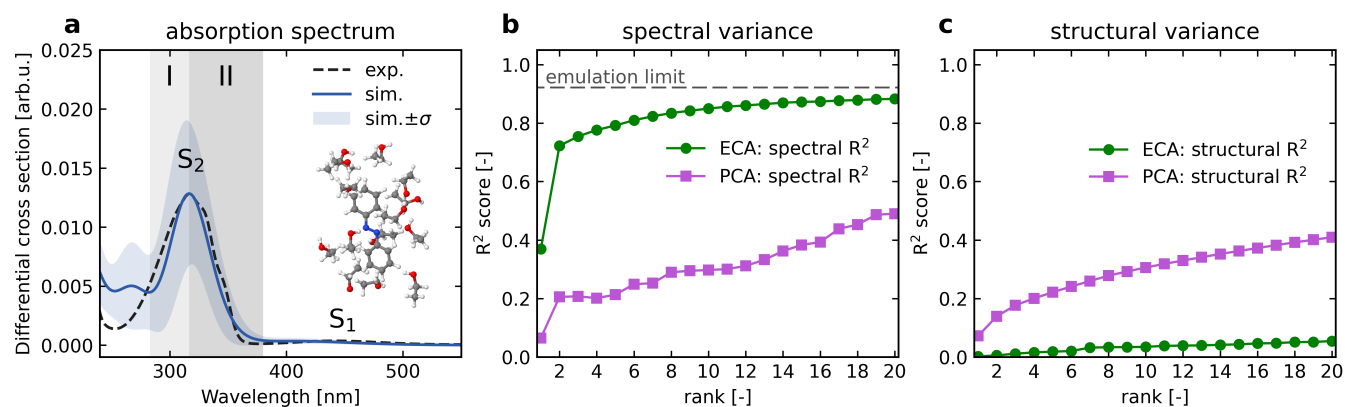


FIG. 10. The corresponding presentation of Figure 1 of the main text, obtained using the PBE functional.

⁴ T. Nägele *et al.*: Femtosecond photoisomerization of cis-azobenzene. *Chemical Physics Letters* 272, 489, 1997.

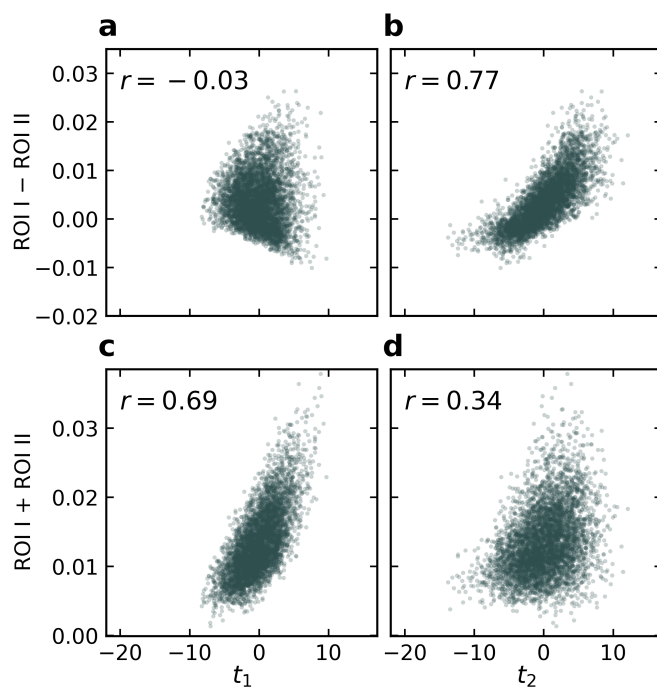


FIG. 11. The corresponding presentation of Figure 2 of the main text, obtained using the PBE functional.

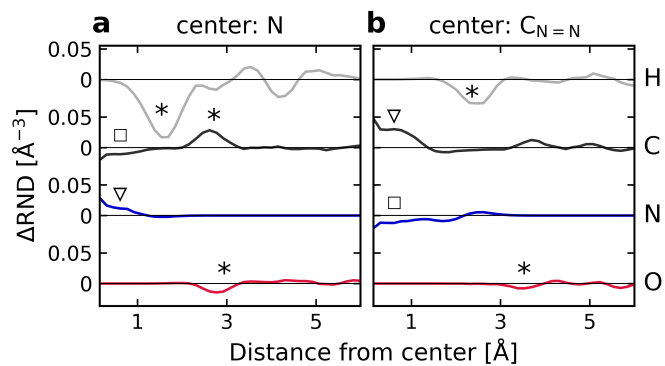


FIG. 12. The corresponding presentation of Figure 3 of the main text, obtained using the PBE functional.

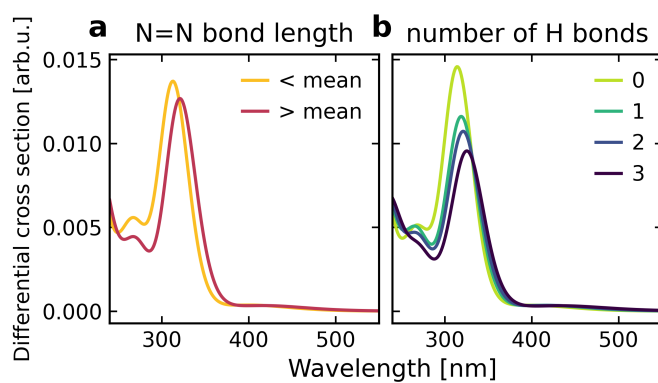


FIG. 13. The corresponding presentation of Figure 4 of the main text, obtained using the PBE functional.